

Carrier Aggregation Enabled Integrated Sensing and Communication Signal Design and Processing

Zhiqing Wei, Haotian Liu, Xinyi Yang, Wangjun Jiang,
Huici Wu, Xingwang Li, Zhiyong Feng

Abstract—The future mobile communication systems will support intelligent applications such as Internet of Vehicles (IoV) and Extended Reality (XR). Integrated Sensing and Communication (ISAC) is regarded as one of the key technologies satisfying the high data rate communication and highly accurate sensing for these intelligent applications in future mobile communication systems. With the explosive growth of wireless devices and services, the shortage of spectrum resources leads to the fragmentation of available frequency bands for ISAC systems, which degrades sensing performance. Facing the above challenges, this paper proposes a Carrier Aggregation (CA)-based ISAC signal aggregating high and low-frequency bands to improve the sensing performance, where the CA-based ISAC signal can use four different aggregated pilot structures for sensing. Then, an ISAC signal processing algorithm with Compressed Sensing (CS) is proposed and the Fast Iterative Shrinkage-Thresholding Algorithm (FISTA) is used to solve the reconfiguration convex optimization problem. Finally, the Cramér-Rao Lower Bounds (CRLBs) are derived for the CA-based ISAC signal. Simulation results show that CA efficiently improves the accuracy of range and velocity estimation.

Index Terms—Carrier aggregation (CA), compressed sensing (CS), high and low-frequency band aggregation, high and low-frequency band cooperative sensing, integrated sensing and communication, Internet of vehicles (IoV), joint communication and sensing, multiple bands radar sensing, multiple bands radar OFDM pilots, signal design, signal processing.

I. INTRODUCTION

The future 5th-Generation-Advanced (5G-A) and 6th-Generation (6G) mobile communication systems will support intelligent applications such as Internet of Vehicles (IoV) and Extended Reality (XR) [1]. These applications require both high data rate communication and highly accurate sensing. Designing a system with both communication and sensing functions is a promising solution to meet the above requirements [2]. With the rapid development of mobile communication systems, the frequency bands of communication systems are rising, which are getting close to the frequency bands of radar systems. Moreover, the signal processing methods and hardware structures of radar and communication systems are similar [3]. Hence, it is feasible to realize the integrated design of radar sensing and communication. The remarkable results of recent researches [3]–[6] show that Integrated Sensing and Communication (ISAC) has the advantages of improving spectrum utilization and reducing device size, which is one of the promising key technologies in 5G-A and 6G.

Since the frequency bands of mobile communication systems are congested, the available spectrum resources for ISAC systems are fragmented, which will degrade the sensing

performance. On one hand, there are deviations in sensing information such as Doppler frequency shifts carried by the echo signals in different frequency bands, making it difficult to directly apply multi-signal accumulation to improve the Signal-to-Noise Ratio (SNR) of the echo signals. On the other hand, when traditional radar sensing algorithms are applied to extract the sensing information from the echo signals on the fragmented spectrum resources, the fragmented spectrum will increase the level of sidelobe and decrease the sensing accuracy [7].

Hence, the efficient aggregation of the fragmented spectrum resources in radar sensing is a great challenge of ISAC signal processing on the congested frequency bands. In the field of communication, Carrier Aggregation (CA) techniques enable the aggregation of fragmented spectrum resources. CA is a spectrum expansion technique adopted by 3rd Generation Partnership Project (3GPP) to alleviate the shortage of contiguous resources. CA could be implemented in physical layer or Media Access Control (MAC) layer, which is divided into two categories, namely physical layer CA and MAC layer CA [8]. In physical layer CA, the selected Component Carriers (CCs) share a common transmission module, where the same modulation and coding techniques are applied. In MAC layer CA, the selected CCs use different transmission modules, where different modulation and coding techniques could be applied depending on the current Channel State Information (CSI) [9]. In terms of communication performance, according to the equation of channel capacity [10], CA significantly improves the channel capacity by increasing the bandwidth. According to [11], [12], in the field of ISAC signal design and processing, it is expected to introduce the idea of CA to aggregate fragmented spectrum resources to improve the resolution and accuracy of radar sensing.

In general, there are three types of CA as shown in Fig. 1, namely intra-band contiguous CA, intra-band non-contiguous CA, and inter-band non-contiguous CA. The intra-band CA is equivalent to transmitting and receiving using larger points of Inverse Fast Fourier Transform (IFFT) and Fast Fourier Transform (FFT), so that the traditional Two-dimensional FFT (2D-FFT) algorithm is still applicable. Towards 5G-A, the sub-6 GHz and millimeter wave (mmWave) spectrum bands are standardized. Furthermore, the full-spectrum will be applied in 6G. Hence, the inter-band non-contiguous CA is widely applied since it realizes more efficient utilization of fragmented spectrum resources via aggregating high and low-frequency bands compared with the other two types of CA. Motivated by this observation, we adopt inter-band non-contiguous CA

TABLE I: Abbreviations and Notations

Abbreviation	Description	Abbreviation	Description
5G-A	5th-Generation-Advanced	6G	6th-Generation
2D	Two-dimensional	3GPP	3rd Generation Partnership Project
AWGN	Additive White Gaussian Noise	ADC	Analog-to-digital converter
BS	Base station	CRLB	Cramér-Rao Lower Bound
CCs	Component Carriers	CSI	Channel state information
CS	Compressed Sensing	CP	Cyclic Prefix
CA	Carrier aggregation	DFT	Discrete Fourier Transform
DAC	Digital-to-analog converter	FFT	Fast Fourier Transform
FISTA	Fast iterative shrinkage-thresholding algorithm	IDFT	Inverse Discrete Fourier Transform
IFFT	Inverse Fast Fourier Transform	ISAC	Integrated sensing and communication
IoV	Internet of Vehicle	IM	Index-modulation
ISI	Inter-symbol interference	LO	Local oscillator
mmWave	Millimeter wave	MAC	Media Access Control
OMP	Orthogonal Matching Pursuit	OFDM	Orthogonal Frequency Division Multiplexing
P/S	Parallel-to-serial conversion	RX	Receiver
RCS	Radar Cross Section	RIP	Restricted Isometry Property
RMSE	Root Mean Square Error	RCRLB	Root Cramér-Rao Lower Bound
S/P	Serial-to-parallel conversion	SNR	Signal-to-Noise Ratio
TX	Transmitter	XR	Extended Reality
Notation	Description	Notation	Description
N	Total number of subcarriers	M	Total number of OFDM symbols
k, K	Interval of comb pilot	q, Q	Interval of block pilot
T_1	Total length of symbols in low-frequency	T_2	Total length of symbols in high-frequency
Δf_1	Subcarrier spacing in low-frequency	Δf_2	Subcarrier spacing in high-frequency
f_{c1}	Carrier frequency in low-frequency	f_{c2}	Carrier frequency in high-frequency
T_{CP}	Length of CP	\mathbf{D}_{cf1}	Channel information matrix in low-frequency
\mathbf{D}_{cf2}	Channel information matrix in high-frequency	R, v_0	Range and velocity of target
\mathbf{Q}, \mathbf{P}	Selection matrix	$(\cdot)^*$	Complex conjugate of the complex number
$(\cdot)^H, (\cdot)^T$	Conjugate transpose, transpose	$\text{vec}(\cdot)$	Stacking matrix in columns
\circ	Hadamard product	\otimes	Kronecker product

to aggregate the fragmented spectrum resources in ISAC signal design and processing. In addition, different types of CA correspond to different architectures of transmitter and receiver. In terms of inter-band CA, according to 3GPP TR 36.912 standard [13], a structure of multi-Radio Frequency (RF) chain is applied in this paper, as shown in Fig. 4. However, the different subcarrier spacing in high and low-frequency bands makes it difficult to directly fuse the sensing information in high and low-frequency bands to improve the sensing performance.

The researches on CA techniques applied to ISAC-enabled mobile communication systems are divided into two cate-

gories, namely the CA-enabled communication and the CA-enabled radar sensing. In terms of CA-enabled communication, Kang *et al.* [15] proposed a broadband high linearity drive amplifier that enables dual carrier aggregation and supports sub-GHz standards. Ginzberg *et al.* [16] proposed a digital linearisation scheme for a dual-channel discontinuous carrier aggregation transmitter which reduces the out-of-band distortion caused by CA. In terms of CA-enabled radar sensing, the radar signal processing for multi-band Orthogonal Frequency Division Multiplexing (OFDM) radar is the most related area. The stepped OFDM radar and frequency-agile stepped OFDM radar adopts the similar techniques in the

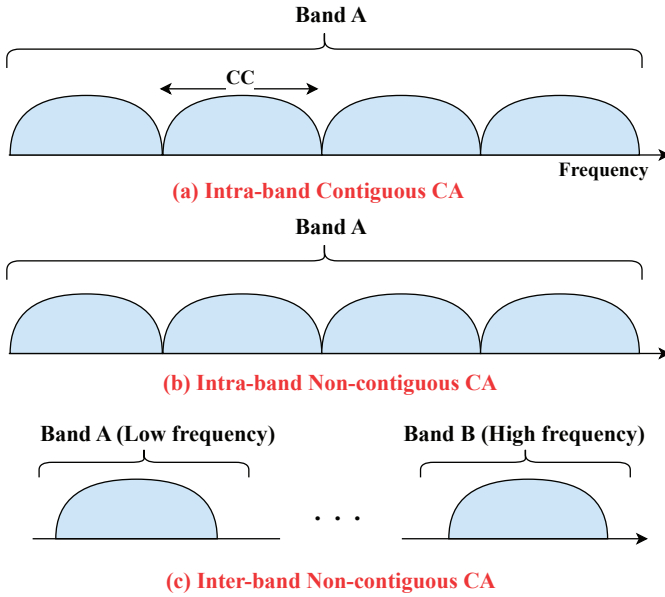


Fig. 1: Three types of CA [14].

intra-band non-contiguous CA. Clemens *et al.* [17] designed a stepped carrier OFDM signal, which combines 20 different frequency bands with 200 MHz bandwidth to form a 4 GHz bandwidth, achieving high range resolution. However, this signal processing method is only suitable for the targets with low mobility. Benedikt *et al.* [18] designed an improved Discrete Fourier Transform (DFT) algorithm that obtains high range and velocity resolution for automotive applications by offsetting the phase errors from the range. In [19], the concept of frequency-agile stepping OFDM is introduced to obtain high range resolution with limited bandwidth and gives a new Doppler processing. Furthermore, Knill *et al.* [20] presented a frequency-agile sparse OFDM radar signal processing method combined with Compressed Sensing (CS) technique to obtain the same sensing performance as equivalent OFDM signal on the continuous spectrum bands without increasing the sampling rate and bandwidth resources. However, the above studies do not involve the aggregation of high and low-frequency bands, where the differentiated subcarrier spacings bring a great challenge for the CA-enabled ISAC signal processing.

The other related research area of CA-based ISAC signal processing is multi-band radar, which improves the sensing accuracy over fragmented frequency bands by reconstructing the data in blank frequency bands. In 1974, Hogbom *et al.* [21] proposed a deconvolution-based method to estimate blank band data and construct a complete two-dimensional (2D) radar image. In 1992, Cuomo [22] introduced the linear predictive Band Width Extrapolation (BWE) technique using an autoregressive time series model to extrapolate bandwidth at blanking positions to achieve high range resolution. In 2004, Suwa *et al.* [23] proposed a Polarisation Band Width Extrapolation (PBWE) technique based on polarised radar data that achieves higher resolution than the conventional BWE technique. In 2009, Stoica *et al.* [24] applied the weighted least

squares Iterative Adaptive Approach (IAA) in radar sensing and proposed a missing data recovery approach applicable to arbitrary data missing patterns. In 2015, Van Khanh *et al.* [25] applied the BWE technique to the Linear Frequency Modulation (LFM) narrow band radar and explored the BWE technique based on Matched Filtering (MF), which results in improved range resolution. In 2016, Zhang *et al.* [26] presented a coherent signal processing and multi-band fusion algorithm based on a sparse signal model, which is adaptable to the case of large spectral spacing between multi-band signals. However, the above studies are oriented for pulsed signal or LFM signal. The study on OFDM signal is very rare in the area of multi-band radar.

In this paper, we propose a CA-based staggered pilot structure for ISAC signal design. With CA techniques, the representative low and high-frequency bands, namely 5.9 GHz [27] and 24 GHz [28] frequency bands are selected as the fusion frequency bands. The parameters of OFDM signals are different in high and low-frequency bands, which brings challenge for the sensing information fusion in different frequency bands. Facing this challenge, the channel information matrix fusion method for CA-based staggered pilot ISAC signal is introduced. Then, a CS-based 2D-FFT algorithm is designed for ISAC signal processing. Finally, the Cramér-Rao Lower Bounds (CRLBs) for the proposed CA-based ISAC signal are derived. The detailed contributions are as follows.

- **CA-based staggered pilot ISAC signal:** The staggered pilot structure is applied for CA-based ISAC signal design, where the block pilot is used in high-frequency band and the comb pilot is used in low-frequency band, which can comprehensively achieve better performance than other CA-based pilot signals.
- **Channel information matrix fusion method:** With the proposed CA-based staggered pilot ISAC signal, the channel information matrix fusion method is proposed to fuse the sensing information in high and low-frequency bands with different parameters of OFDM signal such as subcarrier spacing and length of OFDM symbols.
- **CS-based 2D-FFT algorithm:** The problem of sidelobe elevation and sensing performance degradation caused by the discontinuity of the modified channel information matrix is solved by the proposed CS-based 2D-FFT algorithm, which demonstrates strong anti-noise capability in target sensing.
- **CRLBs of CA-based ISAC Signal:** The CRLBs for velocity and range estimation under the proposed ISAC signal are derived.

The rest of this paper is organized as follows. In Section II, the CA-based staggered pilot signal model is provided. In Section III, the ISAC signal processing methods are proposed. In Section IV, the CRLBs for range and velocity estimation are revealed. In Section V, simulation results are presented. Finally, this paper is summarized in Section VI. Table I shows the abbreviations and notations used in this paper.

II. CARRIER AGGREGATION-BASED ISAC SIGNAL

As shown in Fig. 2, the ISAC system for vehicle communication and sensing is considered. The OFDM signals on 5.9 GHz and 24 GHz frequency bands are representative frequency bands for vehicular communication [29]. Hence, this paper adopts 5.9 GHz and 24 GHz frequency bands to design the CA-based ISAC signal. To make full use of spectrum resources and achieve highly accurate sensing performance, the CA-based staggered pilot ISAC signal is designed.

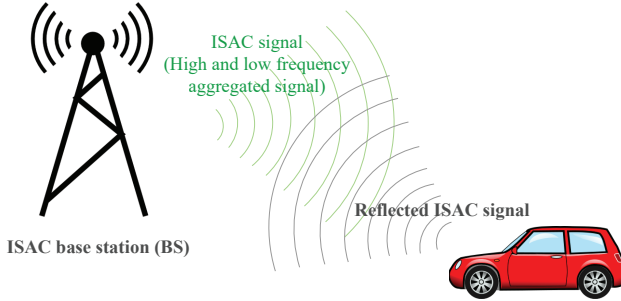


Fig. 2: ISAC base station (BS) for vehicle communication and sensing.

A. The CA-based staggered pilot ISAC signal

As shown in Fig. 3, the structure of the CA-based staggered pilot ISAC signal is provided. Fig. 3(a) represents the structure of block pilot in high-frequency band, which is discrete in time domain and continuous in frequency domain, so that the signal is insensitive to frequency-selective fading. Fig. 3(b) shows the structure of comb pilot in low-frequency band, which is discrete in frequency domain and continuous in time domain. Therefore, the signal is insensitive to time-selective fading.

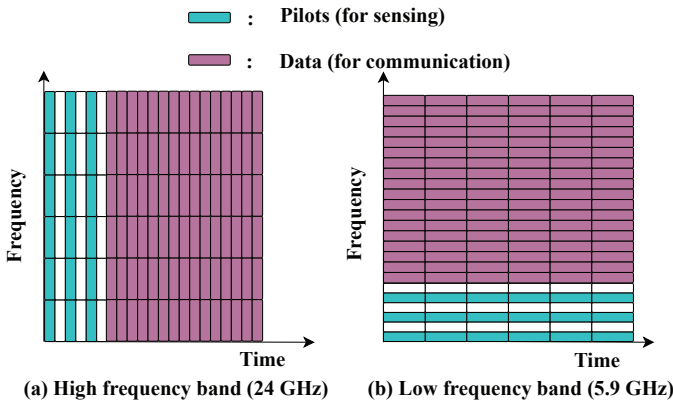


Fig. 3: CA-based staggered pilot ISAC signal.

The comb pilot signal in low-frequency band at the transmitter (TX) is expressed as [30]

$$x_1(t) = \sum_{m=1}^M \sum_{n=1}^{N'} d_{\text{TX1}}(m, kn) \cdot \exp(j2\pi kn \Delta f t), \quad (1)$$

where $N' = N/k$ is the number of subcarriers at the comb pilot location in each OFDM symbol, N is the total number

of subcarriers in each OFDM symbol, and k is the interval of comb pilot. It is noted that $k = \Delta f_2 / \Delta f_1$ is a pre-requisite for the range estimation, where Δf_1 and Δf_2 are the subcarrier spacings in low and high-frequency bands, respectively. Similarly, the time-domain expression of the block pilot signal in the high-frequency band is [31]

$$x_2(t) = \sum_{m=1}^{M'} \sum_{n=1}^N d_{\text{TX2}}(qm, n) \cdot \exp(j2\pi n \Delta f t), \quad (2)$$

where $M' = M/q$ is the number of OFDM symbols at the block pilot location in a frame, M is the total number of OFDM symbols transmitted in one frame of data, and q is the interval of block pilot. According to (1) and (2), the CA-based staggered pilot ISAC signal is expressed as

$$x_{\text{CA1}}(t) = \sum_{m=1}^M \sum_{n=1}^{N'} d_{\text{TX1}}(m, kn) \cdot \exp(j2\pi t (kn \Delta f_1 + f_{c1})) \\ + \sum_{m=1}^{M'} \sum_{n=1}^N d_{\text{TX2}}(qm, n) \cdot \exp(j2\pi t (n \Delta f_2 + f_{c2})), \quad (3)$$

where d_{TX1} and d_{TX2} denote the modulation symbols in low and high-frequency bands, respectively. f_{c1} and f_{c2} represent the carrier frequencies of the low and high-frequency bands, respectively.

The echo signal reflected from the target contains Doppler frequency shift $f_d = 2v/\lambda = 2v f_c / c_0$ and delay $\tau = 2R/c_0$, where R and v are the range and relative velocity of target, respectively, and λ is the wavelength of signal. Therefore, the echo signal at the receiver (RX) after down-conversion is expressed as

$$y(t) = \left(\mathbf{H}_1(m, kn) \sum_{m=1}^M \sum_{n=1}^{N'} d_{\text{TX1}}(m, kn) \cdot e^{j2\pi nk \Delta f_1 (t - \frac{2R}{c_0})} \right. \\ \cdot e^{j2\pi m T_1 \frac{2v f_{c1}}{c_0}} + \mathbf{H}_2(qm, n) \sum_{m=1}^{M'} \sum_{n=1}^N d_{\text{TX2}}(qm, n) \\ \left. \cdot e^{j2\pi nk \Delta f_2 (t - \frac{2R}{c_0})} \cdot e^{j2\pi qm T_2 \frac{2v f_{c2}}{c_0}} \right) + w(t), \quad (4)$$

where $\mathbf{H}_1(m, n)$ and $\mathbf{H}_2(m, n)$ are the channel gain on the n -th subcarrier of the m -th OFDM symbol at high and low-frequency bands, respectively, which consist of channel fading and Radar Cross Section (RCS), $w(t)$ is the Additive White Gaussian Noise (AWGN). T_1 and T_2 represent the total length of the OFDM symbols in low and high-frequency bands, respectively. The symbol length is $T = 1/\Delta f + T_{CP}$, with T_{CP} representing the length of Cyclic Prefix (CP) and Δf representing the subcarrier spacing.

In addition to the above CA-based staggered pilot signal, there are other three aggregated structured signals, which are high-frequency comb and low-frequency block aggregated pilot signal in (5), high and low-frequency full-block aggregated pilot signal in (6), and high and low-frequency full-comb aggregated pilot signal in (7), where the interval of comb pilot

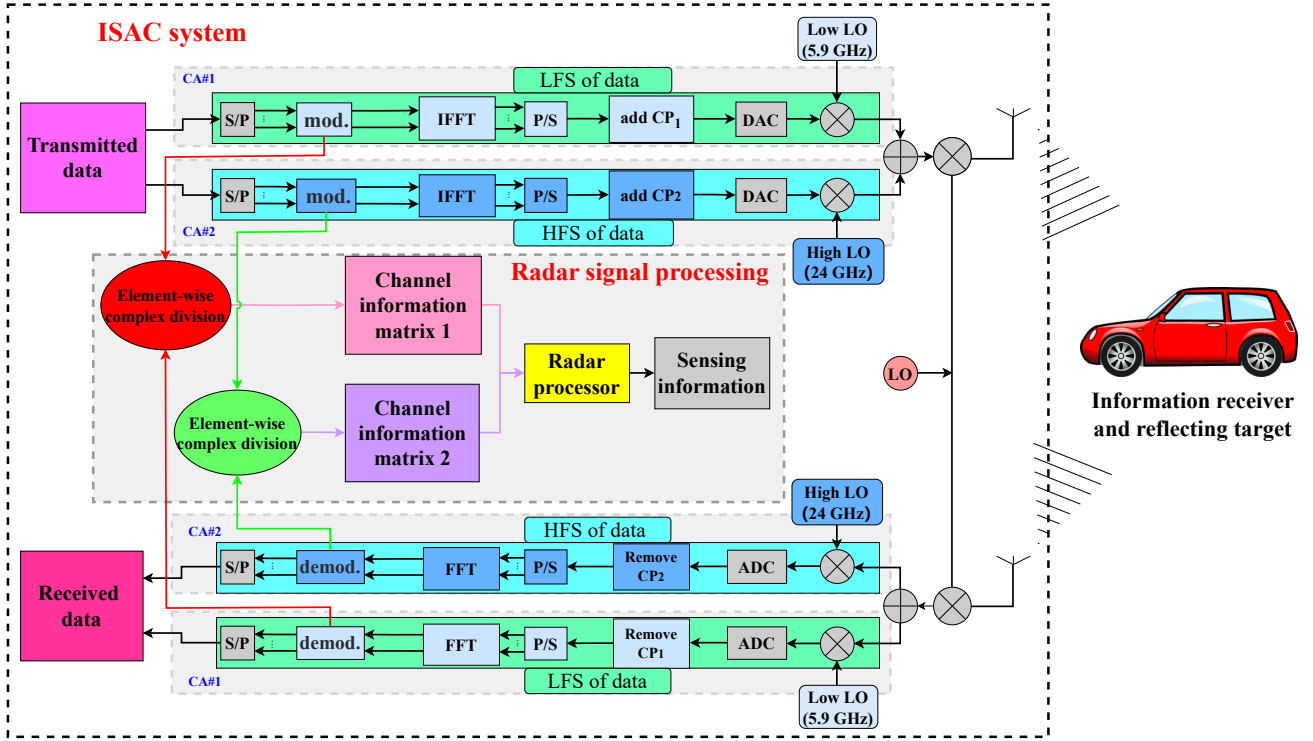


Fig. 4: CA-based ISAC signal processing, with the abbreviations HFS: high-frequency stream, LFS: low-frequency stream, LO: local oscillator, CP: cyclic prefix, FFT: fast Fourier transform, IFFT: inverse fast Fourier transform, ADC: analog-to-digital converter, DAC: digital-to-analog converter, S/P: serial-to-parallel conversion, P/S: parallel-to-serial conversion.

is k , and the interval of block pilot is q .

$$\begin{aligned}
 x_{CA2}(t) &= \sum_{m=1}^{M'} \sum_{n=1}^N d_{TX1}(qm, n) \cdot \exp(j2\pi t(n\Delta f_1 + f_{c1})) \\
 &+ \sum_{m=1}^M \sum_{n=1}^{N'} d_{TX2}(m, kn) \cdot \exp(j2\pi t(kn\Delta f_2 + f_{c2})), \quad (5)
 \end{aligned}$$

$$\begin{aligned}
 x_{CA3}(t) &= \sum_{m=1}^{M'} \sum_{n=1}^N d_{TX1}(qm, n) \cdot \exp(j2\pi t(n\Delta f_1 + f_{c1})) \\
 &+ \sum_{m=1}^{M'} \sum_{n=1}^N d_{TX2}(qm, n) \cdot \exp(j2\pi t(n\Delta f_2 + f_{c2})), \quad (6)
 \end{aligned}$$

$$\begin{aligned}
 x_{CA4}(t) &= \sum_{m=1}^M \sum_{n=1}^{N'} d_{TX1}(m, kn) \cdot \exp(j2\pi t(kn\Delta f_1 + f_{c1})) \\
 &+ \sum_{m=1}^M \sum_{n=1}^{N'} d_{TX2}(m, kn) \cdot \exp(j2\pi t(kn\Delta f_2 + f_{c2})). \quad (7)
 \end{aligned}$$

B. Framework of ISAC signal processing

1) *Signal processing at TX*: As shown in Fig. 4, the transmitted data is divided into two data streams: High-frequency Stream (HFS) and Low-frequency Stream (LFS), which are also denoted by high-frequency CC and low-frequency CC, respectively. In the HFS, the transmitted data is modulated to form a modulated symbol. Undergoing block-wise inverse fast

Fourier transform, subsequent parallel-to-serial conversion and the addition of CP, the signal is converted to an analog signal and mixed with the high-frequency LO signal to provide a high-frequency analog signal [32]. Compared with the HFS, the LFS is mixed with the low-frequency LO to obtain low-frequency analog signal. Then, the low-frequency analog signal and high-frequency analog signal are combined and fed into a single antenna [13]. When the multiple antennas are applied, we need to consider precoding schemes to improve the performance of communication and sensing. Since a single antenna is applied in this paper, the problems associated with multiple antennas are not considered.

2) *Signal processing at RX*: For communication, the demodulation process is similar to traditional OFDM demodulation [33] since the data stream has been separated into HFS and LFS at RX. At the RX, the same steps are performed in reverse order. The received modulated symbol is recovered by FFT. Then, we can also use the traditional maximum likelihood detection to obtain the communication data. For sensing, the modulated symbols at RX are divided by the modulated symbols at TX to obtain the channel information matrix, which is used for radar sensing. A detailed description of the ISAC signal processing is provided in Section III.

The differences in the subcarrier spacings and the length of OFDM symbols in high and low-frequency bands bring challenges for the processing of the CA-based ISAC signal processing, which will be solved in Section III.

III. ISAC SIGNAL PROCESSING

In terms of radar signal processing for OFDM-based ISAC signal, Sturm *et al.* [32] proposed 2D-FFT algorithm, which takes full advantage of the 2D structure of OFDM signal in efficient radar sensing [1]. Zuo *et al.* [34] proposed a CS-based radar signal processing for index-modulated OFDM (OFDM-IM) signals. Based on these previous approaches, we propose a CA-based ISAC signal processing algorithm in this section.

The CS methods apply the sparsity of echo signal to reconstruct the incompletely sampled channel information matrix in 2D-FFT method, thus reducing the Fourier sidelobe deterioration. The channel information matrix is expressed as

$$\mathbf{D} = \mathbf{F}_N \mathbf{X} \mathbf{F}_P^H + \bar{\mathbf{W}}, \quad (8)$$

where \mathbf{X} represents range-velocity profile of target, $\mathbf{F}_N \in \mathbb{C}^{N \times N}$ and $\mathbf{F}_P \in \mathbb{C}^{P \times P}$ are Fourier transform matrices, respectively. N is the total number of subcarriers, P is the number of OFDM symbols, $(\cdot)^H$ is the conjugate transpose of the matrix, $\bar{\mathbf{W}}$ is AWGN matrix. The selection matrix $\mathbf{J} \in \mathbb{C}^{KP \times NP}$ is defined to filter out valid data based on subcarrier activation. The filtering process is shown in Fig. 5. Multiplying both sides of (8) by the matrix \mathbf{J} , we have

$$\mathbf{d} = \mathbf{A} \mathbf{x} + \mathbf{w}, \quad (9)$$

where

$$\begin{cases} \mathbf{d} = \mathbf{J} \text{vec}(\mathbf{D}) \\ \mathbf{A} = \mathbf{J} (\mathbf{F}_P^H \otimes \mathbf{F}_N) \\ \mathbf{x} = \text{vec}(\mathbf{X}) \\ \mathbf{w} = \mathbf{J} \text{vec}(\bar{\mathbf{W}}) \end{cases} \quad (10)$$

In (10), $\text{vec}(\cdot)$ represents stacking matrix in columns, \otimes refers to Kronecker product, \mathbf{A} is the sensing matrix in CS. When \mathbf{x} is a sparse vector and \mathbf{A} satisfies the Restricted Isometry Property (RIP) condition [35], the sparse signals can be reconstructed. Since the solution of (9) is NP-hard, (9) is transformed into (11).

$$\hat{\mathbf{x}} = \arg \min_{\mathbf{x}} \frac{1}{2} \|\mathbf{d} - \mathbf{A} \mathbf{x}\|_2^2 + \lambda \|\mathbf{x}\|_1. \quad (11)$$

Problem (11) is a least square optimization problem that can be solved by the Orthogonal Matching Pursuit (OMP) algorithm. OMP is an iterative greedy algorithm that is utilized to recover high-dimensional sparse signals from a limited number of noisy linear measurements. During each iteration, OMP selects the column that exhibits the highest correlation with the current residual and incorporates it into the set of chosen columns. Detailed descriptions of OMP can be found in [36]. By solving (11), the range-velocity profile is obtained for the complete OFDM signal, avoiding the effect of Fourier sidelobe deterioration.

In this section, the CA-based ISAC signal processing algorithm is proposed, which takes full advantage of the two channel information matrices in high and low-frequency bands, resulting in better sensing performance.

The CA-based staggered pilots signal adopts comb pilot in low-frequency band with interval of $K = \Delta f_2 / \Delta f_1$ and block pilot in high-frequency band with interval of Q . According to Fig. 4, when the low-frequency and high-frequency data

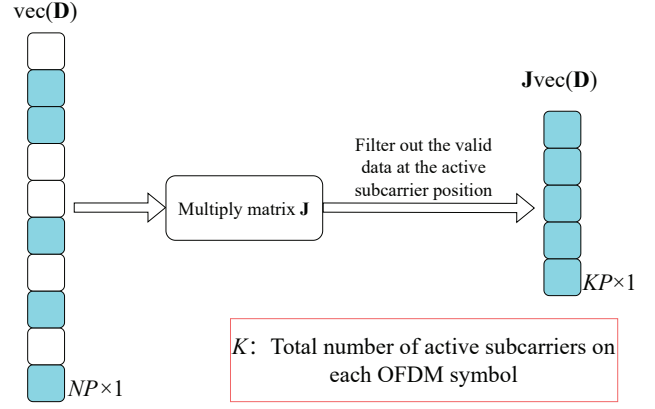


Fig. 5: filtering process using selection matrix \mathbf{J} .

streams pass through the DAC, they are mixed with high and low-frequency LOs to obtain high and low-frequency analog signals. At RX, the mixed high and low-frequency analog signals are separated by matched filtering. Using element-wise complex division, the channel information matrix $\mathbf{D}_{cf1} \in \mathbb{C}^{N \times M}$ in low-frequency band and the channel information matrix $\mathbf{D}_{cf2} \in \mathbb{C}^{N \times M}$ in high-frequency band are obtained at the RX.

$$\begin{aligned} \mathbf{D}_{cf1} &= \mathbf{H}_1(m, n) \circ (k_{r1} \otimes k_{d1}), \\ \mathbf{D}_{cf2} &= \mathbf{H}_2(m, n) \circ (k_{r2} \otimes k_{d2}), \end{aligned} \quad (12)$$

where \circ denotes Hadamard product. Combining the structures of high-frequency block pilot and low-frequency comb pilot, we have

$$\begin{aligned} k_{d1}(m) &= \exp\left(j2\pi m T_1 \frac{2v_0 f_{c1}}{c_0}\right), m = 0, 1, 2, \dots, M-1, \\ k_{r1}(n) &= \exp\left(-j2\pi n \Delta f_1 \frac{2R}{c_0}\right), n = 0, K, 2K, \dots, aK, \end{aligned} \quad (13)$$

where $aK \leq N-1$. And we have

$$\begin{aligned} k_{d2}(m) &= \exp\left(j2\pi m T_2 \frac{2v_0 f_{c2}}{c_0}\right), m = 0, Q, 2Q, \dots, bQ, \\ k_{r2}(n) &= \exp\left(-j2\pi n \Delta f_2 \frac{2R}{c_0}\right), n = 0, 1, 2, \dots, N-1, \end{aligned} \quad (14)$$

where $bQ \leq M-1$. In order to represent the structural form of the two channel information matrices clearly, the matrices are rewritten as (15) and (16), where the elements in \mathbf{D}_{cf1} and \mathbf{D}_{cf2} denote the elements after the division of the received modulation symbols by the transmitted modulation symbols.

A. Range Estimation Method

The different subcarrier spacings in high and low-frequency bands bring challenges for the range estimation using CA-based ISAC signal. According to 2D-FFT algorithm, the column vector of channel information matrix is applied in calculating the range of target [32].

1) *Fusion of channel information matrices*: Comparing (13) and (14), it is discovered that the different parameters between $k_{r1}(n)$ and $k_{r2}(n)$ are n and Δf . As mentioned in

$$\mathbf{D}_{cf1} = \begin{bmatrix} z_{0,0} & z_{0,1} & z_{0,2} & \cdots & z_{0,M-1} \\ 0 & 0 & 0 & \cdots & 0 \\ \vdots & \vdots & \vdots & \ddots & \vdots \\ 0 & 0 & 0 & \cdots & 0 \\ z_{K,0} & z_{K,1} & z_{K,2} & \cdots & z_{K,M-1} \\ 0 & 0 & 0 & \cdots & 0 \\ \vdots & \vdots & \vdots & \ddots & \vdots \\ 0 & 0 & 0 & \cdots & 0 \\ z_{2K,0} & z_{2K,1} & z_{2K,2} & \cdots & z_{2K,M-1} \\ 0 & 0 & 0 & \cdots & 0 \\ \vdots & \vdots & \vdots & \ddots & \vdots \\ 0 & 0 & 0 & \cdots & 0 \\ \vdots & \vdots & \vdots & \ddots & \vdots \\ z_{aK,0} & z_{aK,1} & z_{aK,2} & \cdots & z_{aK,M-1} \\ 0 & 0 & 0 & \cdots & 0 \\ \vdots & \vdots & \vdots & \ddots & \vdots \end{bmatrix}, \quad (15)$$

$$\mathbf{D}_{cf2} = \begin{bmatrix} s_{0,0} & s_{1,0} & s_{2,0} & \cdots & s_{N-1,0} \\ 0 & 0 & 0 & \cdots & 0 \\ \vdots & \vdots & \vdots & \ddots & \vdots \\ 0 & 0 & 0 & \cdots & 0 \\ s_{0,Q} & s_{1,Q} & s_{2,Q} & \cdots & s_{N-1,Q} \\ 0 & 0 & 0 & \cdots & 0 \\ \vdots & \vdots & \vdots & \ddots & \vdots \\ 0 & 0 & 0 & \cdots & 0 \\ s_{0,2Q} & s_{1,2Q} & s_{2,2Q} & \cdots & s_{N-1,2Q} \\ 0 & 0 & 0 & \cdots & 0 \\ \vdots & \vdots & \vdots & \ddots & \vdots \\ 0 & 0 & 0 & \cdots & 0 \\ \vdots & \vdots & \vdots & \ddots & \vdots \\ s_{0,bQ} & s_{1,bQ} & s_{2,bQ} & \cdots & s_{N-1,bQ} \\ 0 & 0 & 0 & \cdots & 0 \\ \vdots & \vdots & \vdots & \ddots & \vdots \end{bmatrix}^T. \quad (16)$$

Section II, $\Delta f_2 = K\Delta f_1$. Replacing the variable n in $k_{r1}(n)$ with Kn' , the transformation of $k_{r1}(n)$ is

$$k_{r1}(n') = \exp\left(-j2\pi n' \left(K\Delta f_1\right) \frac{2R}{c_0}\right), \quad n' = 0, 1, 2, \dots, a, \quad (17)$$

where K is the interval of comb pilot. Comparing $k_{r1}(n')$ in (17) and $k_{r2}(n)$ in (14), $k_{r1}(n')$ is a subsequence of the preceding $a+1$ elements of $k_{r2}(n)$.

2) *CS-based range estimation algorithm*: In order to estimate the range of target, the modulation symbols in high and low-frequency bands at the RX are recovered. Then, the channel information matrix \mathbf{D}_{cf2} in high-frequency band and the channel information matrix \mathbf{D}_{cf1} in low-frequency band are obtained. The elements of \mathbf{D}_{cf1} in the positions of pilot's subcarriers are rearranged, and the channel information matrix \mathbf{D}'_{cf1} is obtained. Finally, in order to overcome the impact of non-continuous subcarriers or symbols on the performance of sensing, the CS-based target estimation method in [34] is applied, which has been introduced at the beginning of Section III. The sensing matrix in [34] needs to be adjusted for non-continuous situations. The process of adjusting the sensing matrices used in this paper is described below. Beck *et al.* proposed the fast iterative shrinkage-thresholding algorithm (FISTA) [37], which applies the gradient descent to solve optimization problems. FISTA achieves fast convergence by generalizing the iterative idea of Nesterov's method [38]. Thus, FISTA is used instead of the OMP reconstruction algorithm to obtain fast convergence speed. The above algorithm is referred to as CS-IDFT. When processing the channel information matrix \mathbf{D}'_{cf1} , a column in the channel information matrix is selected to obtain the sensing matrix based on the location of the valid data in a column. Define a selection matrix $\mathbf{Q} \in \mathbb{C}^{N \times N}$ as follows, where the elements in the first $a+1$

rows are 1 and the rest elements are 0.

$$\mathbf{Q} = \begin{bmatrix} 1_{0,0} & 1_{0,1} & 1_{0,2} & \cdots & 1_{0,N-1} \\ \vdots & \vdots & \vdots & \ddots & \vdots \\ 1_{a,0} & 1_{a,1} & 1_{a,2} & \cdots & 1_{a,N-1} \\ 0 & 0 & 0 & \cdots & 0 \\ \vdots & \vdots & \vdots & \ddots & \vdots \\ 0 & 0 & 0 & \cdots & 0 \end{bmatrix}. \quad (18)$$

The sensing matrix in CS is represented as the product of the sparse basis and the measurement matrix. The channel information matrix can be transformed to the range-Doppler domain under the discrete Fourier transform basis, while the radar signals are generally sparse in the range-velocity domain [20]. Therefore, the sensing matrix in this paper takes the form of Fourier transform basis. $\psi \in \mathbb{C}^{N \times N}$ is the discrete inverse Fourier matrix. Hence, the modified sensing matrix is $\mathbf{Q} \circ \psi^{-1}$. For the remaining columns, the sensing matrix is obtained as (18). Using the sensing matrix and the data in each column of \mathbf{D}'_{cf1} , we can obtain power spectrum of range by solving (11). The range estimation algorithm is shown in Algorithm 1, which is explained intuitively in Fig. 6. The channel information matrix in low-frequency band is firstly processed to obtain the rearranged matrix \mathbf{D}'_{cf1} . Then, the power spectrum of range is obtained using the CS-IDFT algorithm for \mathbf{D}'_{cf1} . The power spectrum of range is obtained using the IDFT of the channel information matrix in high-frequency band. The power spectra of range in high and low-frequency bands are superimposed. Finally, the index value ind_n is obtained by searching the peak of the superimposed power spectrum and the estimated range of target is

$$R = ([ind_n]c_0)/(2\Delta f_2 N). \quad (19)$$

Algorithm 1: Range Estimation Algorithm

Input: Channel information matrix \mathbf{D}_{cf1} in low-frequency band;
Channel information matrix \mathbf{D}_{cf2} in high-frequency band;
Sensing matrix $\mathbf{Q} \circ \psi^{-1}$;
The intervals of comb and block pilots: K and Q ;
The number of OFDM symbols M ;
The number of subcarriers N ;

- 1: **For** the j row vector of \mathbf{D}_{cf1} in steps K **do**
- 2: Initialize a zero matrix $\mathbf{D}'_{cf1} \in \mathbb{C}^{N \times M}$ and $i = 1$;
- 3: Deposit the j row of \mathbf{D}_{cf1} into i -th row of \mathbf{D}'_{cf1} ;
- 4: $i = i + 1$;
- 5: **End For**
- 6: Initialize a power spectrum of range R_r and $\varpi = 0$;
- 7: **For** the j column vector of \mathbf{D}_{cf2} in steps Q **do**
- 8: The result of the IFFT operation on the j -th column of \mathbf{D}_{cf2} is assigned to ϖ ;
- 9: $R_r = R_r + \|\varpi\|$;
- 10: **End For**
- 11: **For** each column vector of \mathbf{D}'_{cf1} **do**
- 12: Input $\mathbf{Q} \circ \psi^{-1}$ and the column vector of \mathbf{D}'_{cf1} to FISTA [37];
- 13: The result of output of the FISTA is assigned to ϖ ;
- 14: $R_r = R_r + \|\varpi\|$;
- 15: **End For**
- 16: Normalize R_r and perform a peak search on it;
- 17: Substitute the index value corresponding to the searched peak into (19);

Output: The estimation of the range \hat{R}

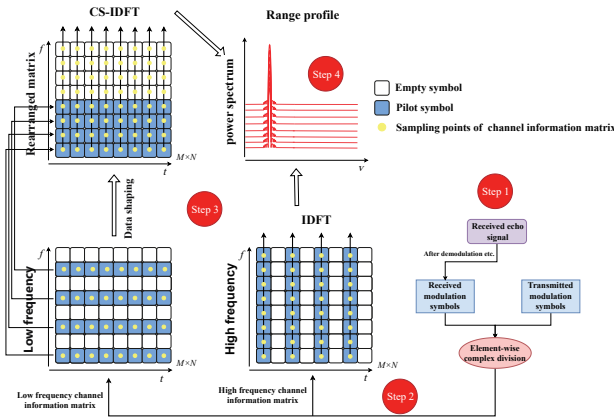


Fig. 6: Signal processing for range estimation.

B. Velocity Estimation Method

In the estimation of target's velocity, the difference in carrier frequencies in high and low-frequency bands leads to different resolutions of the velocity estimation, which brings challenges for the fusion of sensing information in high and low-frequency bands.

1) *Fusion of channel information matrices:* The relative velocity of target introduces a linear phase shift along the time axis, so that only the row vectors of channel information matrix need to be considered.

By observing $k_{d1}(m)$ in (13) and $k_{d2}(m)$ in (14), it is discovered that the different parameters are m , T and f_c . As revealed in Fig. 4, the data streams of HFS and LFS use different modules of adding CP, which can dynamically

adjust CP length. On the premise of meeting the maximum ranging, $T_1 f_{c1} = T_2 f_{c2}$ can be satisfied by adding CP with different lengths. According to 2D-FFT method [32], $ind_m = \lfloor (2v_0 f_c T M) / c_0 \rfloor$ is obtained. Therefore, when the FFT is performed on the row vectors of high and low-frequency channel information matrices, the peak index values will be the same with $T_1 f_{c1} = T_2 f_{c2}$. Therefore, the velocity of target can be estimated by the accumulation of high and low-frequency channel information matrices.

2) *CS-based velocity estimation algorithm:* By observing $k_{d2}(m)$ in (14), it is revealed that the row vector contains the null modulation symbol, and Fourier transform will cause the increase of sidelobe. According to [7], sidelobe and noise can be reduced by the estimation method based on CS. The FISTA reconstruction algorithm is used instead of the OMP algorithm. The algorithm here is referred to CS-DFT. When processing the channel information matrix \mathbf{D}_{cf2} , the sensing matrix for the first row vector in \mathbf{D}_{cf2} is obtained based on the location of the valid data in the first row of \mathbf{D}_{cf2} . A selection matrix $\mathbf{P} \in \mathbb{C}^{M \times M}$ is defined based on the interval of block pilot Q and the number of OFDM symbols M

$$\mathbf{P} = \begin{bmatrix} 1 & 1 & \dots & 1 \\ \vdots & \vdots & \dots & \vdots \\ 1 & 1 & \dots & 1 \\ \vdots & \vdots & \dots & \vdots \end{bmatrix}, \quad (20)$$

where each column of \mathbf{P} is

$$p_{1 \times M} = [1, 0_{1 \times (Q-1)}, 1, 0_{1 \times (Q-1)}, \dots]^T. \quad (21)$$

Then the sensing matrix $\mathbf{P} \circ \psi$ is obtained. For the remaining rows, the sensing matrix is obtained as (20). Using the sensing matrix and the data in each row of \mathbf{D}_{cf2} , the power spectrum of velocity is obtained by solving (11). The velocity estimation algorithm is shown in Algorithm 2, which is explained intuitively in Fig. 7. The power spectrum of velocity is obtained by using the CS-DFT algorithm for the high-frequency channel information matrix. Then, the DFT is performed on the low-frequency channel information matrix according to the pilot position to obtain the power spectrum of velocity. The power spectra of velocity in high and low-frequency bands are superimposed. Finally, the index value ind_m is obtained by searching the peak of the superimposed power spectrum and the estimated velocity of target is

$$v_0 = (\lfloor ind_m \rfloor c_0) / (2f_{c2} T_2 M). \quad (22)$$

IV. PERFORMANCE OF CA-BASED ISAC SIGNAL

In this section, the sensing performance of CA-based ISAC signals is analyzed using Root Mean Square Error (RMSE) and CRLB. Firstly, the ISAC signal processing algorithms under different pilot structures are provided. Then, the CRLBs of ISAC signals under different pilot structures are derived.

A. Other Types of Pilot Structures

The above CA-enabled ISAC signal design adopts the pilot structure with block pilot in high-frequency band and comb

Algorithm 2: Velocity Estimation Algorithm

Input: Channel information matrix \mathbf{D}_{cf1} in low-frequency band;
Channel information matrix \mathbf{D}_{cf2} in high-frequency band;
Sensing matrix $\mathbf{P} \circ \psi$;
The intervals of comb and block pilots: K and Q ;
The number of OFDM symbols M ;
The number of subcarriers N ;

- 1: Initialize a power spectrum of velocity R_v and $\varpi = 0$;
- 2: **For** the j -th row vector of \mathbf{D}_{cf1} in steps K **do**
- 3: The result of the FFT operation for the j -th row of \mathbf{D}_{cf1} is assigned to ϖ ;
- 4: $R_v = R_v + \|\varpi\|$;
- 5: **End For**
- 6: **For** each row vector of \mathbf{D}_{cf2} **do**
- 7: Input $\mathbf{P} \circ \psi$ and the row vector of \mathbf{D}_{cf2} to FISTA [37];
- 8: The result of output of the FISTA is assigned to ϖ ;
- 9: $R_v = R_v + \|\varpi\|$;
- 10: **End For**
- 11: Normalize R_v and perform a peak search on it;
- 12: Substitute the index value corresponding to the searched peak into (22);

Output: The estimation of the range \hat{v}_0

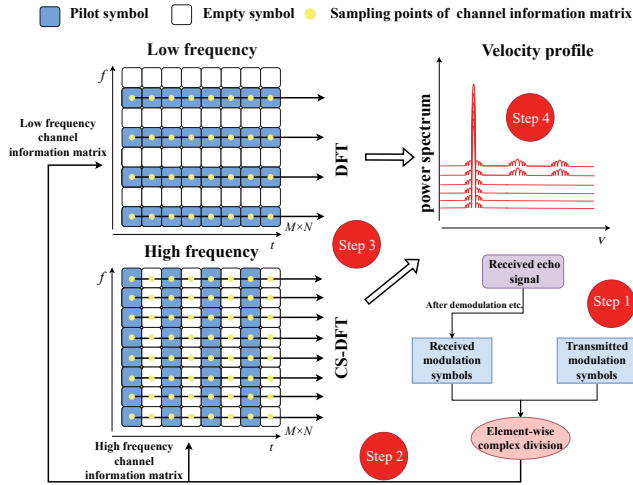


Fig. 7: Signal processing for velocity estimation.

pilot in low-frequency band. However, there are three other pilot structures, which are high-frequency comb and low-frequency block aggregated pilot, high and low-frequency full-block aggregated pilot, and high and low-frequency full-comb aggregated pilot. The signal processing procedures under the other three pilot structures are as follows.

1) *High-frequency comb and low-frequency block aggregated pilot:* The steps of signal processing are as follows.

- **Step 1:** The low-frequency channel information matrix \mathbf{D}_{cf3} and the high-frequency channel information matrix \mathbf{D}_{cf4} are obtained.
- **Step 2:** We perform IDFT on the column vectors corresponding to the block pilot positions of \mathbf{D}_{cf3} , sum the results, search the power spectrum for the peak index value, and combine it with (19) to get the range estimate r_1 . Likewise, we perform CS-DFT on every row vector

of \mathbf{D}_{cf3} , sum the results, combine the peak index value with (22) to get the velocity estimation v_1 .

- **Step 3:** We perform CS-IDFT on every column vector of \mathbf{D}_{cf4} , sum the results, search the power spectrum for the peak index value, and combine it with (19) to get the range estimation r_2 . Likewise, we perform DFT on the row vectors corresponding to the comb pilot positions of \mathbf{D}_{cf4} , sum the results, combine the peak index value with (22) to get the velocity estimation v_2 .
- **Step 4:** We take the average of r_1 and r_2 , and the average of v_1 and v_2 to get the final estimation.

2) *High and low-frequency full-block aggregated pilot:* The steps of signal processing are as follows.

- **Step 1:** The low-frequency channel information matrix \mathbf{D}_{cf5} and the high-frequency channel information matrix \mathbf{D}_{cf6} are obtained.
- **Step 2:** Since both channel information metrics are block-pilot structures, only the processing of \mathbf{D}_{cf5} is provided here and the processing of \mathbf{D}_{cf6} is consistent. We perform IDFT on the column vectors corresponding to the block pilot positions of \mathbf{D}_{cf5} , sum the results, search the power spectrum for the peak index value, and combine it with (19) to get the range estimation r_3 . Likewise, we perform CS-DFT on every row vector of \mathbf{D}_{cf5} , sum the results, combine the peak index value with (22) to get the velocity estimation v_3 . Then, the same process is performed on \mathbf{D}_{cf6} to get r_4 and v_4 .
- **Step 3:** We take the average of r_3 and r_4 , and the average of v_3 and v_4 to get the final estimation.

3) *High and low-frequency full-comb aggregated pilot:* The steps of signal processing are as follows.

- **Step 1:** The low-frequency channel information matrix \mathbf{D}_{cf7} and the high-frequency channel information matrix \mathbf{D}_{cf8} are obtained.
- **Step 2:** Since both channel information metrics are comb-pilot structures, only the processing of \mathbf{D}_{cf7} is provided here, and the processing of \mathbf{D}_{cf8} is consistent. We perform CS-IDFT on every column vector of \mathbf{D}_{cf7} , sum the results, search the power spectrum for the peak index value, and combine it with (19) to get the range estimation r_5 . Likewise, we perform DFT on the row vectors corresponding to the comb pilot positions of \mathbf{D}_{cf7} , sum the results, combine the peak index value with (22) to get the velocity estimation v_5 . Then, the same process is performed on \mathbf{D}_{cf8} to get r_6 and v_6 .
- **Step 3:** We take the average of r_5 and r_6 , and the average of v_5 and v_6 to get the final estimation.

To verify the superiority of the staggered pilot structure chosen in this paper, the RMSE performance of various pilot structures is compared in Section V.

B. CRLBs of Various Pilot Structures

The CRLBs of CA-enabled ISAC signals under different pilot structures are derived. It is noted that since the carrier frequencies in high and low-frequency bands are different and the estimator of Doppler frequency shift $f_d = 2v_0 f_c / c_0$ contains the carrier frequency f_c . To facilitate theoretical

derivation, we take out the carrier frequency f_c and set the estimator as $\theta = 2v_0/c_0$. In this way, when performing the derivation, we do not have to pay attention to the effect of the different carrier frequencies in high and low-frequency bands. The received echo signal at RX can be expressed as

$$y_{m,n} = h_{m,n} e^{j2\pi m T_s f_c \theta} e^{-j2\pi n \Delta f \tau} + \omega_{m,n}, \quad (23)$$

where $h_{m,n}$ denotes the product of the channel attenuation factor and the amplitude of transmitted signal, $\omega_{m,n} \sim \mathcal{N}(0, \sigma^2)$ is the AWGN, m represents the index of m -th symbol, and n represents the index of n -th subcarrier. It is revealed that τ and θ are unknown in the received echo signal, which contain the range and velocity information of target. Therefore, joint estimation of parameters τ and θ is required. The log-likelihood function is

$$\begin{aligned} \ln p(y; \tau, \theta) = & -\frac{MN}{2} \ln(2\pi\sigma^2) \\ & -\frac{1}{2\sigma^2} \sum_m \sum_n (y_{m,n} - s_{m,n})^* (y_{m,n} - s_{m,n}), \end{aligned} \quad (24)$$

where $(\cdot)^*$ denotes the complex conjugate of the complex number and

$$\begin{aligned} p(y; \tau, \theta) = & \frac{1}{(2\pi\sigma^2)^{MN/2}} \\ & \cdot e^{-\frac{1}{2\sigma^2} \sum_m \sum_n |y_{m,n} - h_{m,n} e^{j2\pi m T_s f_c \theta} e^{-j2\pi n \Delta f \tau}|^2} \\ s_{m,n} = & h_{m,n} e^{j2\pi m T_s f_c \theta} e^{-j2\pi n \Delta f \tau}. \end{aligned} \quad (25) \quad (26)$$

The first derivative of τ and θ can be expressed as

$$\begin{aligned} \frac{\partial \ln p(y; \tau, \theta)}{\partial \tau} = & \frac{-1}{2\sigma^2} \sum_m \sum_n \\ & \cdot [(y_{m,n} - s_{m,n})^* (s_{m,n}) - (y_{m,n} - s_{m,n})(s_{m,n})^*] (j2\pi n \Delta f), \end{aligned} \quad (27)$$

$$\begin{aligned} \frac{\partial \ln p(y; \tau, \theta)}{\partial \theta} = & \frac{1}{2\sigma^2} \sum_m \sum_n \\ & \cdot [(y_{m,n} - s_{m,n})^* (s_{m,n}) - (y_{m,n} - s_{m,n})(s_{m,n})^*] (j2\pi m T_s f_c). \end{aligned} \quad (28)$$

The second derivative of τ is

$$\begin{aligned} \frac{\partial^2 \ln p(y; \tau, \theta)}{\partial \tau^2} = & -\frac{1}{2\sigma^2} \sum_m \sum_n (j2\pi n \Delta f) \\ & \cdot \left[(y_{m,n}^* - s_{m,n}^*) \frac{\partial s_{m,n}}{\partial \tau} - (s_{m,n}) \frac{\partial s_{m,n}^*}{\partial \tau} \right. \\ & \left. - (y_{m,n} - s_{m,n}) \frac{\partial s_{m,n}^*}{\partial \tau} + (s_{m,n}^*) \frac{\partial s_{m,n}}{\partial \tau} \right]. \end{aligned} \quad (29)$$

Upon taking the negative expectation of (29), we have

$$\begin{aligned} F_{1,1} = & -E \left(\frac{\partial^2 \ln p(y; \tau, \theta)}{\partial \tau^2} \right) \\ = & \frac{1}{2\sigma^2} \sum_m \sum_n (j2\pi n \Delta f) \left[(-s_{m,n}) \frac{\partial s_{m,n}^*}{\partial \tau} + (s_{m,n}^*) \frac{\partial s_{m,n}}{\partial \tau} \right] \\ = & \frac{1}{\sigma^2} \sum_m \sum_n (2\pi n \Delta f)^2 h_{m,n}^2. \end{aligned} \quad (30)$$

Similarly, the negative expectation of the second derivative

of θ can be obtained

$$\begin{aligned} F_{2,2} = & -E \left(\frac{\partial^2 \ln p(y; \tau, \theta)}{\partial \theta^2} \right) \\ = & \frac{1}{\sigma^2} \sum_m \sum_n (2\pi m T_s f_c)^2 h_{m,n}^2, \end{aligned} \quad (31)$$

$$\begin{aligned} F_{1,2} = F_{2,1} = & -E \left(\frac{\partial^2 \ln p(y; \tau, \theta)}{\partial \tau \partial \theta} \right) \\ = & \frac{-1}{\sigma^2} \sum_m \sum_n (2\pi)^2 h_{m,n}^2 m n \Delta f T_s f_c. \end{aligned} \quad (32)$$

Then, the Fisher information matrix can be derived as

$$\begin{aligned} \mathbf{F}^{-1} = & \begin{bmatrix} CRLB(\tau) & CRLB(\tau, \theta) \\ CRLB(\theta, \tau) & CRLB(\theta) \end{bmatrix} \\ = & \begin{bmatrix} F_{1,1} & F_{1,2} \\ F_{2,1} & F_{2,2} \end{bmatrix}^{-1}, \end{aligned} \quad (33)$$

and

$$\begin{aligned} CRLB(\tau) = & \frac{F_{2,2}}{F_{1,1}F_{2,2} - F_{1,2}F_{2,1}} \\ = & \frac{\sigma^2}{(2\pi)^2 h_{m,n}^2} \cdot \frac{1}{\sum_m \sum_n (n \Delta f)^2 - \frac{(\sum_m \sum_n m n \Delta f T_s f_c)^2}{\sum_m \sum_n (m T_s f_c)^2}}, \end{aligned} \quad (34)$$

$$\begin{aligned} CRLB(\theta) = & \frac{F_{1,1}}{F_{1,1}F_{2,2} - F_{1,2}F_{2,1}} \\ = & \frac{\sigma^2}{(2\pi)^2 h_{m,n}^2} \cdot \frac{1}{\sum_m \sum_n (m T_s f_c)^2 - \frac{(\sum_m \sum_n m n \Delta f T_s f_c)^2}{\sum_m \sum_n (n \Delta f)^2}}. \end{aligned} \quad (35)$$

According to the transformation relation of $\tau = 2R/c_0$ and $\theta = 2v/c_0$, the CRLBs of range and velocity estimation are

$$CRLB(R) = \frac{c_0^2}{4} CRLB(\tau), \quad (36)$$

$$CRLB(v) = \frac{c_0^2}{4} CRLB(\theta). \quad (37)$$

1) *CRLB of CA-based staggered pilot signal:* According to Section III, the interval of comb pilot satisfies $K = \Delta f_2/\Delta f_1$, so that we have $\Delta f_1 K = \Delta f_2$ in the derivation of CRLB. According to (34) and (36), the CRLB of range estimation $CRLB(R)$ is

$$\begin{aligned} CRLB(R) = & \frac{c_0^2}{4} \\ & \cdot \frac{\sigma^2}{(2\pi)^2 h_{m,n}^2} \cdot \frac{1}{\sum_m \sum_n (n \Delta f)^2 - \frac{(\sum_m \sum_n m n \Delta f T_s)^2}{\sum_m \sum_n (m T_s)^2}}. \end{aligned} \quad (38)$$

Then, combining with the process of Algorithm 1, the sum in (38) is the sum of two channel information matrices in high and low-frequency bands. Therefore,

$$\begin{aligned} & \sum_{m=0}^{M-1} \sum_{n=0}^{N_\alpha-1} (nK \Delta f_1)_{\text{Low}}^2 + \sum_{m=0}^{M_\beta-1} \sum_{n=0}^{N-1} (n \Delta f_2)_{\text{High}}^2 = \\ & \frac{MN_\alpha(N_\alpha-1)(2N_\alpha-1)\Delta f_1^2 K^2}{6} + \frac{M_\beta N(N-1)(2N-1)\Delta f_2^2}{6}, \end{aligned} \quad (39)$$

$$CRLB(R)_1 = \left[\frac{3c_0^2\sigma^2}{8\pi^2\Delta f_2^2 h_{m,n}^2} \right. \\ \left. MN_\alpha(N_\alpha-1)(2N_\alpha-1) + M_\beta N(N-1)(2N-1) - \frac{9[N_\alpha(N_\alpha-1)M(M-1) + N(N-1)M_\beta(M_\beta-1)Q]^2}{4[N_\alpha M(M-1)(2M-1) + NQ^2 M_\beta(M_\beta-1)(2M_\beta-1)]} \right]. \quad (42)$$

$$CRLB(v)_1 = \left[\frac{3c_0^2\sigma^2}{8\pi^2 f_{c1}^2 T_1^2 h_{m,n}^2} \right. \\ \left. N_\alpha M(M-1)(2M-1) + NQ^2 M_\beta(M_\beta-1)(2M_\beta-1) - \frac{9[N_\alpha(N_\alpha-1)M(M-1) + N(N-1)M_\beta(M_\beta-1)Q]^2}{4[MN_\alpha(N_\alpha-1)(2N_\alpha-1) + M_\beta N(N-1)(2N-1)]} \right]. \quad (43)$$

$$CRLB(R)_2 = \left[\frac{3c_0^2\sigma^2}{8\pi^2 h_{m,n}^2} \right. \\ \left. \Delta f_2^2 K^2 MN_\alpha(N_\alpha-1)(2N_\alpha-1) + \Delta f_1^2 M_\beta N(N-1)(2N-1) - \frac{9[\Delta f_2 K N_\alpha(N_\alpha-1)M(M-1) + \Delta f_1 N(N-1)M_\beta(M_\beta-1)Q]^2}{4[N_\alpha M(M-1)(2M-1) + NQ^2 M_\beta(M_\beta-1)(2M_\beta-1)]} \right]. \quad (45)$$

$$CRLB(v)_2 = \left[\frac{3c_0^2\sigma^2}{8\pi^2 f_{c1}^2 T_1^2 h_{m,n}^2} \right. \\ \left. N_\alpha M(M-1)(2M-1) + NQ^2 M_\beta(M_\beta-1)(2M_\beta-1) - \frac{9[\Delta f_2 K N_\alpha(N_\alpha-1)M(M-1) + \Delta f_1 N(N-1)M_\beta(M_\beta-1)Q]^2}{4[\Delta f_2^2 K^2 MN_\alpha(N_\alpha-1)(2N_\alpha-1) + \Delta f_1^2 M_\beta N(N-1)(2N-1)]} \right]. \quad (46)$$

$$\sum_{m=0}^{M-1} \sum_{n=0}^{N_\alpha-1} (mT_1 f_{c1})_{\text{Low}}^2 + \sum_{m=0}^{M_\beta-1} \sum_{n=0}^{N-1} (mQT_2 f_{c2})_{\text{High}}^2 = \\ \frac{N_\alpha M(M-1)(2M-1)T_1^2 f_{c1}^2}{6} + \frac{NQ^2 M_\beta(M_\beta-1)(2M_\beta-1)T_2^2 f_{c2}^2}{6}, \quad (40)$$

$$\sum_{m=0}^{M-1} \sum_{n=0}^{N_\alpha-1} (mnK\Delta f_1 T_1 f_{c1})_{\text{Low}} + \sum_{m=0}^{M_\beta-1} \sum_{n=0}^{N-1} (mQn\Delta f_2 T_2 f_{c2})_{\text{High}} = \\ = \frac{\Delta f_1 K T_1 f_{c1} N_\alpha(N_\alpha-1)M(M-1)}{4} + \frac{\Delta f_2 T_2 f_{c2} N(N-1)M_\beta(M_\beta-1)Q}{4}, \quad (41)$$

where $N_\alpha = N/K$ is the number of subcarriers occupied by the pilot in low-frequency band, $M_\beta = M/Q$ is the number of OFDM symbols occupied by the pilot in high-frequency band. By substituting (39), (40), and (41) into (38), the CRLB of range estimation of CA-based staggered pilot signal is (42).

In terms of velocity estimation, $T_1 f_{c1} = T_2 f_{c2}$ is known using Algorithm 2, so that only one pair of parameters, namely T_1 and f_{c1} , are selected when deriving CRLB. Firstly, (44) can be obtained according to (35) and (37).

$$CRLB(v) = \frac{c_0^2}{4} \cdot \frac{\sigma^2}{(2\pi)^2 h_{m,n}^2} \cdot \frac{1}{\sum_m \sum_n (mT_s f_c)^2 - \frac{(\sum_m \sum_n mn\Delta f T_s f_c)^2}{\sum_m \sum_n (n\Delta f)^2}}. \quad (44)$$

Then, according to Algorithm 2, the sum in (44) is the sum of two channel information matrices in high and low-frequency bands. Similarly, substituting (39), (40), and (41) into (44), the CRLB of velocity estimation of the CA-based staggered pilot ISAC signal is shown in (43).

The CRLBs for the CA-enabled ISAC signals under the remaining pilot structures are provided as follows. For the simplicity in deriving the CRLBs, the comb pilot intervals

of low and high-frequency bands are set the same, which is denoted by K . Meanwhile, the block pilot intervals of low and high-frequency bands are set the same, denoting by Q .

2) *CRLB with high-frequency comb and low-frequency block aggregated pilot*: Similarly, the CRLBs for range and velocity estimation are given by (45) and (46), respectively.

3) *CRLB with high and low-frequency full-block aggregated pilot*: The CRLBs for range and velocity estimation are given by (47) and (48), respectively.

4) *CRLB with high and low-frequency full-comb aggregated pilot*: The CRLBs for range and velocity estimation are given by (49) and (50), respectively.

V. SIMULATION RESULTS AND ANALYSIS

In this section, the power spectrum and RMSE of radar sensing are simulated to verify the feasibility and performance of the proposed CA-based ISAC signal design and processing methods. Then, the RMSEs and CRLBs of the four pilot structures are simulated.

Firstly, we assume that the maximum unambiguous velocity of sensing is $v = 50$ m/s. The subcarrier spacing in the 5.9 GHz low-frequency band is 30 kHz, while the subcarrier spacing in the 24 GHz high-frequency band is 120 kHz according to the 3GPP TS 38.211 standard [40] and subcarrier spacing design principle in [39]. With the farthest detection distance 200 m, the length of CP must be greater than the maximum multipath delay spread, so that the length of CP must be greater than $1.33 \mu\text{s}$ and there is no inter-symbol interference (ISI). The parameters in simulation are summarized in Table II, which satisfies the scenario of vehicle communication and sensing.

A. Performance of Radar Sensing

In this subsection, the feasibility and sensing performance of the proposed ISAC signal processing algorithm are verified

$$CRLB(R)_3 = \frac{\frac{3c_0^2\sigma^2}{8\pi^2 h_{m,n}^2}}{N(N-1)M_\beta \left[(\Delta f_1^2 + \Delta f_2^2)(2N-1) - \frac{9(\Delta f_1 + \Delta f_2)^2(N-1)(M_\beta-1)}{8(2M_\beta-1)} \right]}. \quad (47)$$

$$CRLB(v)_3 = \frac{\frac{3c_0^2\sigma^2}{8\pi^2 f_{c1}^2 T_1^2 h_{m,n}^2}}{NM_\beta(M_\beta-1) \left[2(2M_\beta-1) - \frac{9(\Delta f_1 + \Delta f_2)^2(N-1)(M_\beta-1)}{4(\Delta f_1^2 + \Delta f_2^2)(2N-1)} \right]}. \quad (48)$$

$$CRLB(R)_4 = \frac{\frac{3c_0^2\sigma^2}{8\pi^2 \Delta f_2^2 h_{m,n}^2}}{N_\alpha(N_\alpha-1)M \left[(2N_\alpha-1)(K^2+1) - \frac{9(1+K)^2(N_\alpha-1)(M-1)}{8(2M-1)} \right]}. \quad (49)$$

$$CRLB(v)_4 = \frac{\frac{3c_0^2\sigma^2}{8\pi^2 f_{c1}^2 T_1^2 h_{m,n}^2}}{N_\alpha(M-1)M \left[2(2M-1) - \frac{9(1+K)^2(N_\alpha-1)(M-1)}{4(1+K^2)(2N_\alpha-1)} \right]}. \quad (50)$$

TABLE II: Parameter Configuration of ISAC System based on CA [20], [39], [40].

Symbol	Parameter	Low frequency	High frequency
f_c	Carrier frequency	5.9 GHz	24 GHz
M	Number of OFDM symbols	64	64
N	Number of subcarriers	512	512
K	Comb pilot interval	4	4
Q	Block pilot interval	4	4
Δf	Subcarrier spacing	30 kHz	120 kHz
T	Total OFDM symbol duration	39.5 μ s	9.7 μ s
B	Bandwidth of signal	15.4 MHz	61.4 MHz

by simulating the power spectrum and RMSE of radar sensing according to the parameters in Table II. The power spectra for range and velocity estimation are simulated with the range of target 117 m, the relative velocity of target 30 m/s and the SNR 10 dB, as shown in Fig. 8 and Fig. 9, respectively. X and Y in the figure are used to indicate the peak and the corresponding index value. As the power spectrum is normalized, so that it corresponds to the peak position when Y = 1. According to the indexes of the peaks of the power spectra, the target's range and velocity are estimated as follows.

$$\hat{R} = \frac{(ind_n - 1)c_0}{2\Delta f N} = 117.1875 \text{ m}, \quad (51)$$

$$\hat{v}_0 = \frac{(ind_m - 1)c_0}{2f_{c2}T_2M} = 30.3176 \text{ m/s}, \quad (52)$$

where $ind_n = 49$ and $ind_m = 4$ represent the peak index value of the power spectra of range and velocity, respectively.

It is revealed that the error of range estimation is 0.1875

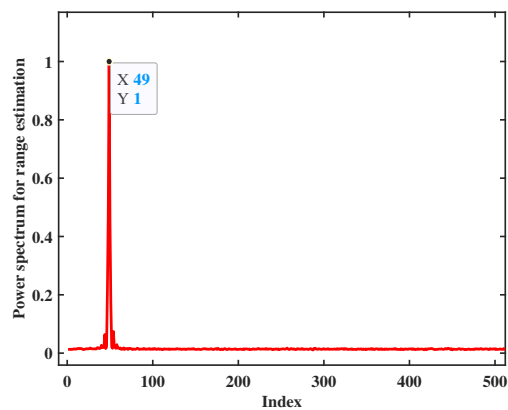


Fig. 8: Power spectrum of range.

m and the error of velocity estimation is 0.3176 m/s. Then, RMSE is used to reveal the deviation between the estimated

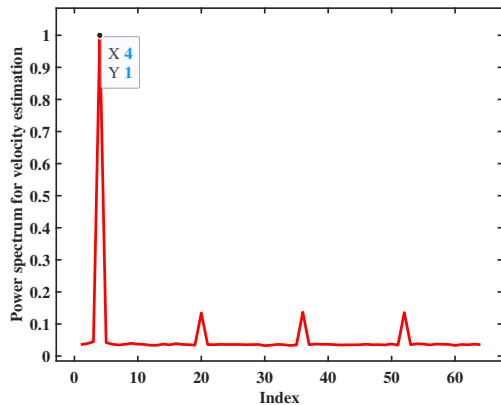


Fig. 9: Power spectrum of velocity.

value and the real value. The performance of range and velocity estimation using high-frequency signal is better than that using low-frequency signal. Meanwhile, the block pilot signal performs better in range estimation and the comb pilot signal performs better in velocity estimation. Hence, the CA-based staggered pilot signal is compared with high-frequency block pilot signal in range estimation and is compared with high-frequency comb pilot signal in velocity estimation to verify the performance improvement using CA.

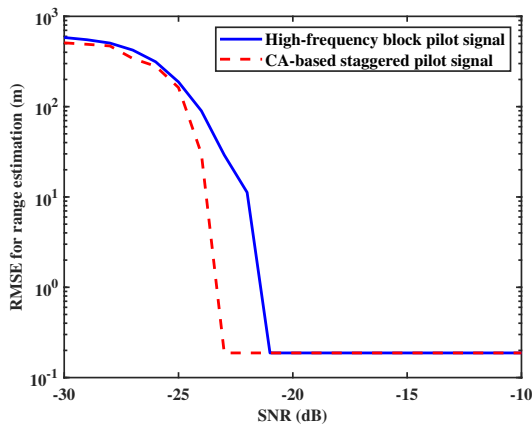


Fig. 10: RMSE for the range.

The RMSE of the high-frequency signal and the CA-based staggered pilot signal for range and velocity estimation are shown in Fig. 10 and Fig. 11, respectively. It is revealed that the RMSEs of the range and velocity estimation with the proposed ISAC signal, namely the CA-based staggered pilot signal, are smaller than those with high-frequency block pilot signal and high-frequency comb pilot signal, respectively. Hence, the CA-based staggered pilot signal has better anti-noise capability and sensing performance than the signals without CA.

B. CRLB of Range and Velocity Estimation

The CRLBs of CA-based staggered pilot ISAC signals is simulated. Then, the comparison of Root CRLBs (abbreviated

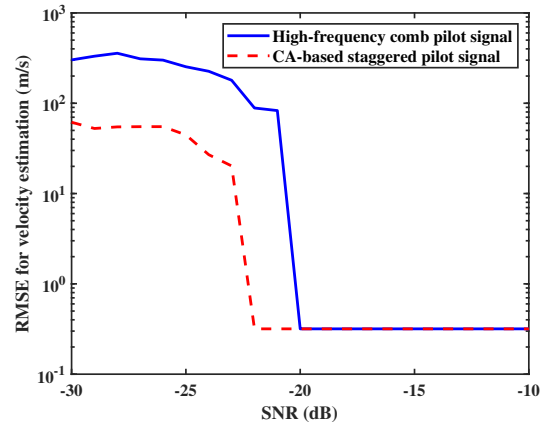


Fig. 11: RMSE for the velocity.

as RCRLBs) and RMSE is simulated based on the parameters in Table II.

1) *CRLB analysis*: As shown in Fig. 12, when the SNR is fixed, the CRLB of range estimation is decreasing with the increase of the CRLB of velocity estimation, namely, the CRLBs of range and velocity estimation have a tradeoff relation. The reason is that the CRLB of velocity estimation is proportional to the subcarrier spacing, whereas the CRLB of range estimation is inversely proportional to the subcarrier spacing. Besides, when the subcarrier spacing is fixed, the CRLBs of range and velocity estimation are decreasing with the increase of SNR.

2) *CRLB comparison*: Fig. 13 and Fig. 14 show the comparison of RCRLB and RMSE for range and velocity estimation, respectively. It is observed that the RCRLB is smaller than the RMSE because the RCRLB reveals the lower bound of the minimum root variance of unbiased estimation. Meanwhile, the 2D-FFT algorithm has a fixed resolution due to the fixed sampling rate and number of FFT points in the simulation, causing the RMSE to converge to a fixed value in the high SNR regime.

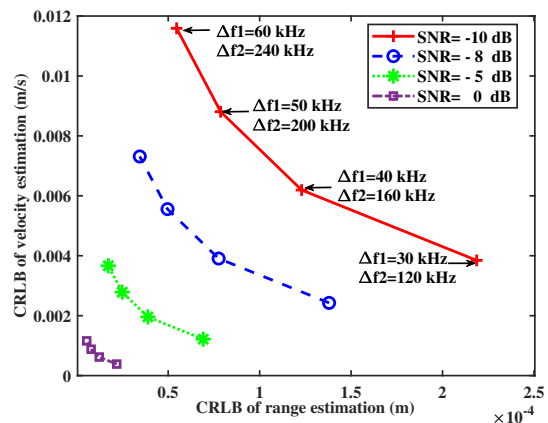


Fig. 12: CRLB for range and velocity with different subcarrier spacing and different SNR.

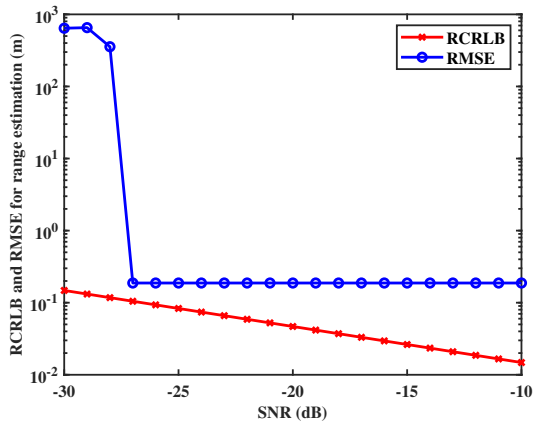


Fig. 13: Comparison of RCRLB and RMSE for range.

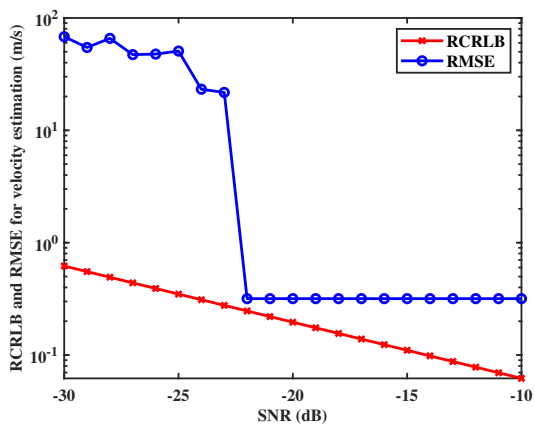


Fig. 14: Comparison of RCRLB and RMSE for velocity.

C. Simulation Comparison of Four Pilot Structures

In this subsection, we simulate the RMSEs and CRLBs for four pilot structures based on the parameters in Table II.

1) *CRLBs of four pilot structures*: According to (42) - (50), the CRLBs for range and velocity estimation with the four pilot structures are shown in Fig. 15 and Fig. 16, respectively. As revealed in Fig. 15, the CA-based staggered pilot has the lowest CRLB. Therefore, when the ISAC-enabled mobile communication system is mainly used to obtain high-accurate range estimation of target, the CA-based staggered pilot structure is the optimal choice. In terms of velocity estimation, as shown in Fig. 16, the high and low-frequency full-comb aggregated pilot has the lowest CRLB, followed by the CA-based staggered pilot. It is observed that the gap of the CRLBs between the low-frequency full-comb aggregated pilot and the CA-based staggered pilot is small. Therefore, when the ISAC-enabled mobile communication system is mainly used to obtain high-accurate velocity estimation of target, both the high and low-frequency full-comb aggregated pilot and the CA-based staggered pilot structure can be chosen.

CRLB comparisons are performed theoretically. In practice, the sensing performance of various pilot structures depends on the signal processing algorithms. Therefore, in the following, we simulate the RMSE of four pilot structures using the

algorithm proposed in this paper.

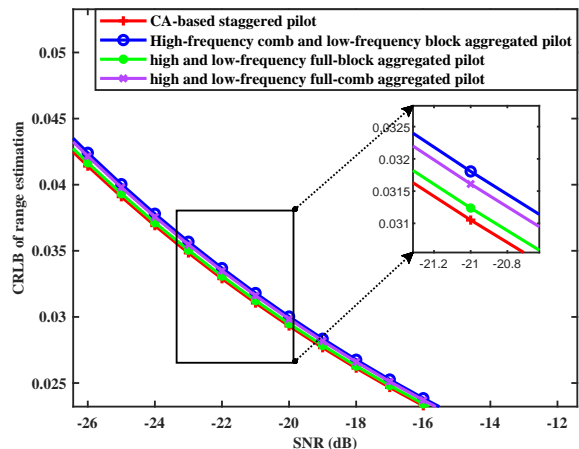


Fig. 15: Range CRLB simulation comparison diagram of four aggregation types.

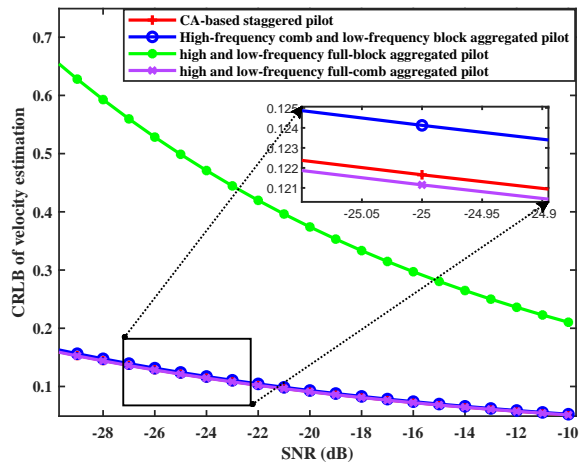


Fig. 16: Velocity CRLB simulation comparison diagram of four aggregation types.

2) *RMSEs of four pilot structures*: The RMSEs for range and velocity estimation with the four pilot structures are shown in Fig. 17 and Fig. 18, respectively. As revealed in Fig. 17, the CA-based staggered pilot has the fastest convergence speed among the four pilot structures. When the SNR is large than the threshold -22 dB, the RMSE of range estimation with the CA-based staggered pilot remains constant. While the thresholds of SNR with other pilot structures are smaller than -22 dB. Hence, in terms of range estimation, the CA-based staggered pilot has the best performance among the four pilot structures.

In terms of velocity estimation, as shown in Fig. 18, the CA-based staggered pilot has the fastest convergence speed among the four pilot structures. When the SNR is larger than the threshold -22 dB, the RMSE of velocity estimation with CA-based staggered pilot is converged to a constant value. While the thresholds of SNR with other pilot structures are smaller than -22 dB. Therefore, the CA-based staggered pilot has the best velocity estimation performance among the four pilot structures.

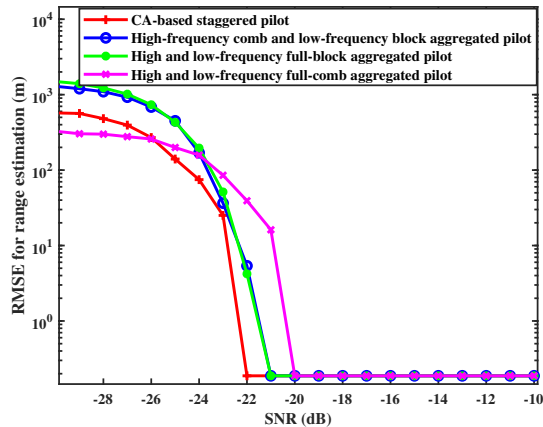


Fig. 17: Range RMSE simulation comparison diagram of four aggregation types.

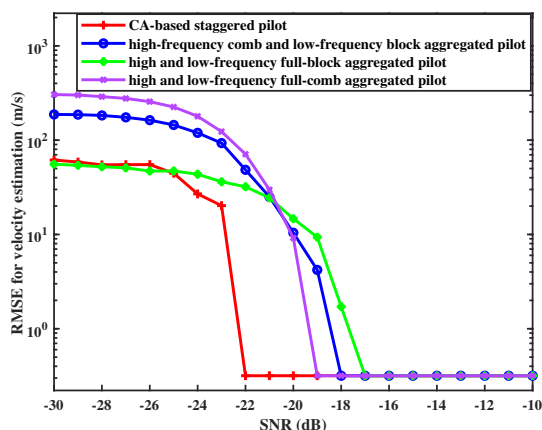


Fig. 18: Velocity RMSE simulation comparison diagram of four aggregation types.

VI. CONCLUSION

This paper proposes the CA-based ISAC signals to improve sensing performance by aggregating discontinuous high and low-frequency bands. Then, the radar signal processing algorithms based on 2D-FFT and CS are proposed, which fuse the sensing information from high and low-frequency bands. The CRLBs of range and velocity estimation with the proposed ISAC signals are analyzed. The feasibility and performance improvement of the ISAC signals proposed in this paper are verified by simulation results. It is revealed that the CA-based ISAC signal has better sensing performance compared with the ISAC signal without CA. Since the full spectrum is one of the promising key technologies in 6G, which efficiently aggregates the low and high-frequency bands to provide high communication data rate, the CA-enabled ISAC signals proposed in this paper may provide a guideline for the ISAC system design in the era of 6G. The future research problems focus on the sensing algorithms with different path losses on high and low frequency bands and the effect of nonlinear high-frequency power amplifier of transmitter RF.

REFERENCES

- [1] Z. Wei, H. Qu, Y. Wang, X. Yuan, H. Wu, Y. Du, K. Han, N. Zhang, and Z. Feng, "Integrated Sensing and Communication Signals Towards 5G-A and 6G: A Survey," *IEEE Internet of Things Journal*, Jan 2023.
- [2] P. Kumari, J. Choi, N. González-Prelcic, and R. W. Heath, "IEEE 802.11 ad-Based Radar: An Approach to Joint Vehicular Communication-Radar System," *IEEE Transactions on Vehicular Technology*, vol. 67, no. 4, pp. 3012–3027, Nov 2017.
- [3] Z. Feng, Z. Fang, Z. Wei, X. Chen, Z. Quan, and D. Ji, "Joint radar and communication: A survey," *China Communications*, vol. 17, no. 1, pp. 1–27, Jan 2020.
- [4] Z. Wang, K. Han, J. Jiang, Z. Wei, G. Zhu, Z. Feng, J. Lu, and C. Meng, "Symbiotic Sensing and Communications Towards 6G: Vision, Applications, and Technology Trends," in *2021 IEEE 94th Vehicular Technology Conference (VTC2021-Fall)*. IEEE, Dec 2021, pp. 1–5.
- [5] S. Li, W. Yuan, C. Liu, Z. Wei, J. Yuan, B. Bai, and D. W. K. Ng, "A Novel ISAC Transmission Framework Based on Spatially-Spread Orthogonal Time Frequency Space Modulation," *IEEE Journal on Selected Areas in Communications*, vol. 40, no. 6, pp. 1854–1872, Mar 2022.
- [6] W. Yuan, Z. Wei, S. Li, J. Yuan, and D. W. K. Ng, "Integrated Sensing and Communication-Assisted Orthogonal Time Frequency Space Transmission for Vehicular Networks," *IEEE Journal of Selected Topics in Signal Processing*, vol. 15, no. 6, pp. 1515–1528, Oct 2021.
- [7] G. Huang, "Research on Modulation Techniques for Fusion of Radar and Communications," Ph.D. dissertation, Guilin University Of Electronic Technology, Jun 2021.
- [8] Carrier Aggregation explained. [Online]. Available: <https://www.3gpp.org/technologies/101-carrier-aggregation-explained>
- [9] R. Ratasuk, D. Toli, and A. Ghosh, "Carrier Aggregation in LTE-Advanced," in *2010 IEEE 71st Vehicular Technology Conference*. IEEE, Jun 2010, pp. 1–5.
- [10] A. Goldsmith, *Wireless communications*. Cambridge university press, 2005.
- [11] R. Thomä, T. Dallmann, S. Jovanoska, P. Knott, and A. Schmeink, "Joint communication and radar sensing: An overview," in *2021 15th European Conference on Antennas and Propagation (EuCAP)*. IEEE, Mar 2021, pp. 1–5.
- [12] T. Wild, V. Braun, and H. Viswanathan, "Joint design of communication and sensing for beyond 5G and 6G systems," *IEEE Access*, vol. 9, pp. 30 845–30 857, Feb 2021.
- [13] 3GPP, "Feasibility Study for Further Enhancements for E-UTRA (LTE Advanced) (Release 9)," 3rd Generation Partnership Project (3GPP), Technical Report (TR) 36.912, Sep 2009.
- [14] H. Lee, S. Vahid, and K. Moessner, "A Survey of Radio Resource Management for Spectrum Aggregation in LTE-Advanced," *IEEE Communications Surveys & Tutorials*, vol. 16, no. 2, pp. 745–760, Nov 2013.
- [15] D.-W. Kang and J.-H. Choi, "A dual-path high linear amplifier for carrier aggregation," *ETRI Journal*, vol. 42, no. 5, pp. 773–780, Oct 2020.
- [16] N. Ginzberg, T. Gidoni, and E. Cohen, "Carrier Aggregation Transmitter Linearization using 2D-DPD and Out-of-Band IM3 Cancellation," in *2022 IEEE Topical Conference on RF/Microwave Power Amplifiers for Radio and Wireless Applications (PAWR)*. IEEE, Jan 2022, pp. 76–78.
- [17] C. Pfeffer, R. Feger, and A. Stelzer, "A stepped-carrier 77-GHz OFDM MIMO radar system with 4 GHz bandwidth," in *2015 European Radar Conference (EuRAD)*. IEEE, Dec 2015, pp. 97–100.
- [18] B. Schweizer, C. Knill, D. Schindler, and C. Waldschmidt, "Stepped-Carrier OFDM-Radar Processing Scheme to Retrieve High-Resolution Range-Velocity Profile at Low Sampling Rate," *IEEE Transactions on Microwave Theory and Techniques*, vol. 66, no. 3, pp. 1610–1618, Sep 2017.
- [19] G. Lellouch, P. Tran, R. Pribic, and P. Van Genderen, "OFDM waveforms for frequency agility and opportunities for Doppler processing in radar," in *2008 IEEE Radar Conference*. IEEE, Dec 2008, pp. 1–6.
- [20] C. Knill, B. Schweizer, S. Sparrer, F. Roos, R. F. Fischer, and C. Waldschmidt, "High Range and Doppler Resolution by Application of Compressed Sensing Using Low Baseband Bandwidth OFDM Radar," *IEEE Transactions on Microwave Theory and Techniques*, vol. 66, no. 7, pp. 3535–3546, Jun 2018.
- [21] J. Hogbom and I. Carlsson, "Observations of the structure and polarization of intense extragalactic radio sources at 1415 MHz," *Astronomy and Astrophysics*, vol. 34, pp. 341–354, Sep 1974.
- [22] K. M. Cuomo, "A Bandwidth Extrapolation Technique for Improved Range Resolution of Coherent Radar Data. Revision 1," Massachusetts Inst of Tech Lexington Lincoln Lab, Tech. Rep., Dec 1992.

- [23] K. Suwa and M. Iwamoto, "Bandwidth extrapolation technique for polarimetric radar data," IEICE transactions on communications, vol. 87, no. 2, pp. 326–334, Feb 2004.
- [24] P. Stoica, J. Li, J. Ling, and Y. Cheng, "Missing Data Recovery Via a Nonparametric Iterative Adaptive Approach," in 2009 IEEE International Conference on Acoustics, Speech and Signal Processing. IEEE, Feb 2009, pp. 3369–3372.
- [25] V. K. Nguyen and M. D. D. Turley, "Bandwidth extrapolation of LFM signals for narrowband radar systems," IEEE Transactions on Aerospace and Electronic Systems, vol. 51, no. 1, pp. 702–712, Jan 2015.
- [26] H. H. Zhang and R. S. Chen, "Coherent processing and superresolution technique of multi-band radar data based on fast sparse Bayesian learning algorithm," IEEE Transactions on Antennas and Propagation, vol. 62, no. 12, pp. 6217–6227, Oct 2014.
- [27] L. Cheng, B. E. Henty, D. D. Stancil, F. Bai, and P. Mudalige, "Mobile vehicle-to-vehicle narrow-band channel measurement and characterization of the 5.9 GHz dedicated short range communication (DSRC) frequency band," IEEE journal on selected areas in communications, vol. 25, no. 8, pp. 1501–1516, Oct 2007.
- [28] H. Zhang, L. Li, and K. Wu, "24GHz Software-Defined Radar System for Automotive Applications," in 2007 European Conference on Wireless Technologies. IEEE, Dec 2007, pp. 138–141.
- [29] P. Zhao, "Range and Velocity Measurement Using OFDM Signal in Typical Vehicle Communication Environment," Master's thesis, Hunan University, May 2014.
- [30] C. D. Ozkaptan, E. Ekici, O. Altintas, and C.-H. Wang, "OFDM Pilot-based Radar for Joint Vehicular Communication and Radar Systems," in 2018 IEEE Vehicular Networking Conference (VNC). IEEE, Jan 2018, pp. 1–8.
- [31] X. Chen, "Research on vehicle-mounted radar range and velocity measurement method based on ofdm pilot signal," Master's thesis, Hunan University, May 2015.
- [32] C. Sturm and W. Wiesbeck, "Waveform Design and Signal Processing Aspects for Fusion of Wireless Communications and Radar Sensing," Proceedings of the IEEE, vol. 99, no. 7, pp. 1236–1259, May 2011.
- [33] S. C. Thompson, A. U. Ahmed, J. G. Proakis, J. R. Zeidler, and M. J. Geile, "Constant envelope OFDM," IEEE transactions on communications, vol. 56, no. 8, pp. 1300–1312, Aug 2008.
- [34] J. Zuo, R. Yang, X. Li, and D. Li, "A Compressed Sensing Method for Joint Radar and Communication System Based on OFDM-IM Signal," Journal of Electronics and Information Technology, no. 2976-2983, Dec 2020.
- [35] M. A. Davenport, M. F. Duarte, Y. C. Eldar, and G. Kutyniok, "Introduction to Compressed Sensing," in Compressed Sensing: Theory and Applications. Cambridge University Press, 2012, pp. 1–64.
- [36] T. T. Cai and L. Wang, "Orthogonal Matching Pursuit for Sparse Signal Recovery With Noise," IEEE Transactions on Information theory, vol. 57, no. 7, pp. 4680–4688, Jul 2011.
- [37] A. Beck and M. Teboulle, "A fast iterative shrinkage-thresholding algorithm for linear inverse problems," SIAM journal on imaging sciences, vol. 2, no. 1, pp. 183–202, 2009.
- [38] Y. E. Nesterov, "A method of solving a convex programming problem with convergence rate $O\left(\frac{1}{k^2}\right)$," in Doklady Akademii Nauk, vol. 269, no. 3. Russian Academy of Sciences, 1983, pp. 543–547.
- [39] M. Braun, C. Sturm, A. Niethammer, and F. K. Jondral, "Parametrization of joint OFDM-based radar and communication systems for vehicular applications," in 2009 IEEE 20th International Symposium on Personal, Indoor and Mobile Radio Communications. IEEE, Apr 2009, pp. 3020–3024.
- [40] 3GPP, "NR; Physical channels and modulation," 3rd Generation Partnership Project (3GPP), Technical Specification (TS) 38.211, vol. 9, 2018.